High-resolution modelling of methane plumes: validation and sensitivity experiments to explore emission quantification approaches

Rakesh Yuvaraj, Thomas Lauvaux, Charbel Abdallah, Philippe Ciais, Julian Akani Guery, Jean-Louis Bonne, Alexis Groshenry, Ngoc Minh Hoang, Lilian Joly

High-resolution modelling of methane plumes: validation and sensitivity experiments to explore emission quantification approaches

Rakesh Yuvaraj*[1,2], Thomas Lauvaux[1,2], Charbel Abdallah[1], Philippe Ciais[2], Julian Akani Guery[3], Jean-Louis Bonne[1], Alexis Groshenry[3,4], Ngoc Minh Hoang[1], and Lilian Joly[1]

[1] *Groupe de Spectrométrie Moléculaire et Atmosphérique (GSMA), Université de Reims-Champagne Ardenne, UMR CNRS 7331, 51100 Reims, France*
[2] *Laboratoire des Sciences du Climat et de l'Environnement (LSCE), IPSL, CEA-CNRS-UVSQ, Université Paris-Saclay, 91191 Gif sur Yvette Cedex, France*
[3] *Kayrros SAS, 75009 Paris, France*
[4] *QAIrbon, 06130 Grasse, France*

Abstract

Methane (CH_4) emissions from natural gas, waste, and industrial sources are routinely detected by satellite and aerial platforms; however, quantifying these plumes remains challenging due to their complex structure and rapidly changing fine-scale atmospheric dynamics. This study directly addresses the resulting uncertainties in UAV flight measurements by employing the Fire Dynamics Simulation (FDS) in Large Eddy Simulation (LES) mode, leveraging mean wind data derived from LiDAR datasets. The FDS model was validated with in-situ CH_4 concentration data collected by Uncrewed Aerial Vehicles (UAVs) during controlled release experiments. Our analysis of ten extensively sampled plumes shows that FDS accurately reproduces the magnitude and spatiotemporal variations of the observed plumes for sufficiently large pipes (diameter > 0.6 cm). We found that factors such as gas exit velocity, obstacles, and terrain topography significantly affect the near-field dynamics of the plumes. To a lesser extent, the temperature of the gas influences plume behaviour at higher mass-flow rates. We highlight the added value of high-resolution LES modelling to understand CH_4 plume dynamics captured by various sensors, aiming to improve current emissions quantification methods.

Keywords: Large Eddy Simulations modelling, methane leaks, high-resolution turbulence, UAV sampling, plume dynamics

Synopsis: Accurately simulating methane leaks requires high-resolution plume simulations that consider terrain topology, obstacles (such as buildings and forests), and gas exit velocity at short-range.

1 Introduction

The global atmospheric methane (CH_4) concentration has been on a steady ascent since the pre-industrial era, soaring from 1750 ppb to an alarming 1912 ppb by 2022[1]. While the overall trend re-

flects a dramatic rise in atmospheric CH_4 over the last few centuries, the past few decades have revealed significant shifts in terms of sources and sinks. Lauvaux et al. [2] highlight that while large and ultra-large oil and gas emitters account for only 8–12 % of the global methane budget, a vast number of smaller emitters—often undetectable by low-resolution global satellites—follow a power-law distribution up to 100 kg h^{-1} [3]. Williams et al. [4] show that of the 500 estimated facility-level emissions considered, 61 % of the emissions come from sources smaller than 50 kg h^{-1}. While the Climate and Clean Air Coalition [5] highlights the significant and rapid potential of reducing greenhouse gas emissions by targeting large-scale sources, previous studies increasingly reveal that the aggregate of small-scale emissions also contributes substantially to the global greenhouse gas budget, underscoring the critical importance of high-resolution modelling for accurate assessment and effective mitigation strategies.

Quantifying methane emissions encompasses the use of multispectral and hyperspectral imagery from aircraft and satellites for large-scale sources [6,7], complemented by precise in-situ measurements near smaller sources [8,9]. Short-term fluctuations in emissions and smaller leaks (<100 kg_{CH_4} h^{-1}) can be challenging to detect and monitor using satellites due to limitations in detection thresholds, resolution, precision, cloud cover, and satellite overpass frequency. To address these challenges, UAVs are utilised, allowing for close-range monitoring—typically within tens of metres from the emission source—and the ability to capture the vertical profile of the plume.

Bonne et al. [9] detail an experiment in which they measured controlled methane emissions from various sources at different times of day, employing a mass-balance algorithm to estimate the emission rate. Similarly, Morales et al. [10] describe a controlled release experiment of methane sampled by instruments mounted on a UAV flying transects perpendicular to the wind direction at a specific distance from the source, at multiple altitudes. Han et al. [11] describe a novel air sampler mounted on a UAV, and employed Gaussian plume inversion methods for emission estimation, achieving strong agreement with mass-balance methods. Yong et al. [12] discuss the turbulent nature of methane plumes from landfills and account for the invalidity of the assumption that the wind field and methane plume are constant during a single flight. Dooley et al. [13] describe the deployment of UAVs to measure CH_4 and C_2H_6, to distinguish biogenic and thermogenic sources. Hu et al. [14] show the comparison of good agreement between observation (OGI camera and LI-COR instrument) and WRF-GHG LES simulations; however, they point out that the OGI camera was limited by weather conditions, such as the camera's failure to measure at early hours near sunrise due to colder temperatures.

Methane plumes in the atmosphere are essentially turbulent owing to the velocity of release, the velocity of the free-stream air, and the temperature difference between the ground and the air. The turbulence intensity depends on the time of day, season, and complexity of terrain topology. To understand the flow, it is required to resolve turbulence at all scales. In Large Eddy Simulations (LES), however, the turbulence from large scales (of the order of the flow domain) up to the scale given by the simulation's resolution is calculated exactly, and all the sub-grid-scale (SGS) physics is calculated using different SGS models [15,16]. In the present work, the smallest scales are of the order of the methane emission source, and the large scales are chosen to accommodate the sampling planes away from the edge of the domain boundary.

On average, the turbulent kinetic energy contained in the large-scale structures breaks down into small-scale structures. This method works best when the large-scale motion of methane dominates the flow dynamics due to the large emission. Although large-scale methane plumes have

been observed at many sites around the globe[17], most leaks tend to be detected at short distances from the source, driven by small-scale turbulence, accumulating over time to represent a significant fraction of the total gas emitted per day per industrial sector[18]. The solution is to use Large Eddy Simulations (LES), which solves the exact Navier-Stokes equation for the large scales in the flow and uses turbulent closure schemes to simulate the SGS dynamics of the flow[19,20,21,22,23].

To assess the validity of the LES model, it is necessary to compare an existing experimental measured dataset with the known emission rate (as in the case of controlled releases) using a UAV to see how close we can replicate the variability of the measured datasets with fluid simulations. In this study, we validate the Fire Dynamics Simulation (FDS) model through controlled methane releases and subsequently investigate various parameters that influence the dynamics of the methane plume. Section 2 provides a detailed description of the controlled release experiments and UAV flights, followed by an overview of the key aspects of FDS relevant to this work. Section 3 presents the evaluation of the simulations, along with a sensitivity analysis of the parameters affecting our LES. Finally, Section 4 discusses the critical factors driving the performance of the LES model.

2 Methods

2.1 UAV measurements during controlled release experiments

We used atmospheric CH_4 concentrations from UAV measurement campaigns collected over the TADI (Total Anomaly Detection Initiatives) platform at PERL (Pôle d'études et de Recherche de Lacq) between October 1 and 10, 2019. Located in southwestern France (43.41 °N, 0.64 °W), this 2000 m^2 site features a mostly flat landscape surrounded by rural communities and agricultural land.

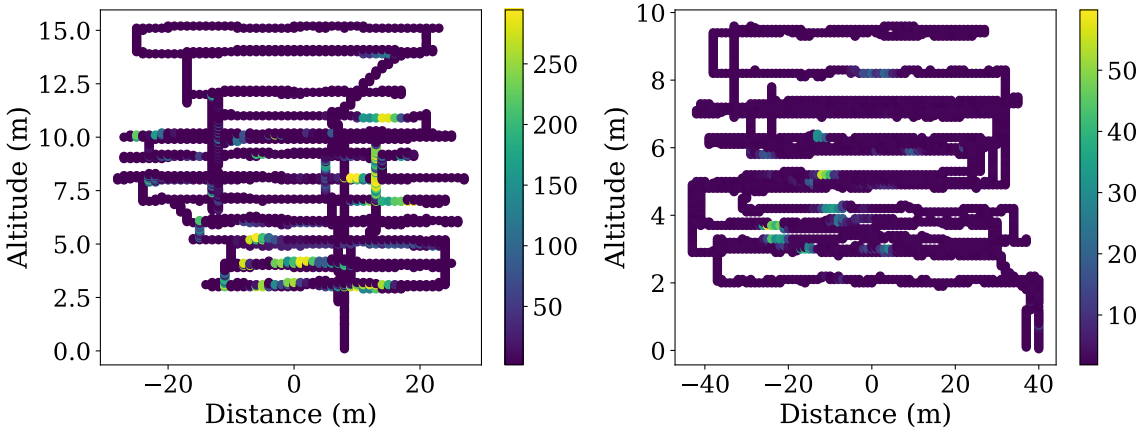

Figure 1: Two examples of the observed atmospheric CH_4 concentrations collected during UAV flights, showing multiple horizontal transects at various altitudes. The transects are collected perpendicular to the mean wind direction, downstream of the controlled release source. The colorbar shows methane concentration enhancements (ΔCH_4) in ppm.

The TADI site includes multiple pipelines to release natural gas at varying flow rates and heights, ranging from 0.1 m to 6.5 m above ground level, distributed across the area. During the measurement campaign, the instrument onboard the UAV recorded specific quantities of CO_2 and

CH_4 emitted at different times of the day. Atmospheric concentrations were measured by the Airborne Ultra-light Spectrometer for Environmental Application (AUSEA)[24,25]. Each release lasted between 600 s and 4380 s, with 300 s pauses in between. A commercial ZX300 Doppler wind lidar (from ZX Lidars Inc.) measured the wind speed and directions at 10 different elevations between 11 m and 300 m above ground level (AGL). For further details about the TADI platform, refer to Kumar et al.[8],[26], for information about the AUSEA instrument, please refer to S1, and for information specific to the measurement campaign used in this study, see Bonne et al.[9].

Figure 1 shows the UAV transects from two different flights (a large release and a small release), measuring sources at different intensities at different altitudes. For the present comparison, we chose ten flights from the sixty-seven flights of the measurement campaign. These flights were selected based on their high Signal-to-Noise Ratio (SNR) of CH_4 enhancement. The selection was further constrained to UAV flights with 10 m wind speed between 3-5 m s^{-1}, CH_4 exit velocity $\geq$ 1.7 m s^{-1}, and a sufficient number of UAV transects perpendicular to the wind. To simulate the different plumes with FDS, we also collected the information of mass flow rate, diameter, and height of the release of the source from the experiments, converted it into a mass flux (in kg_{CH_4} $m^{-2}s^{-1}$), and gave it as input to FDS.

2.2 FDS configuration

Fire Dynamics Simulation (FDS) is a Computational Fluid Dynamics (CFD) model specifically designed for fluid flows driven by fire. FDS solves the Navier-Stokes equation for low-speed (Mach number < 0.3), thermally-driven flow with a focus on the transport of smoke and heat emanating from fires. In its development, FDS has focused on solving practical fire safety problems in fire protection engineering by providing a tool to study the fundamentals of fire and combustion. Therefore, most of the applications of FDS revolve around smoke handling systems, sprinkler/detector activation studies, and reconstructions of residential and industrial fires[27,28,29]. More information on FDS is given in Supporting Information S2.

Our study employs FDS (LES) to simulate CH_4 plumes. The primary goal is to validate the modelled methane concentration enhancement by comparing it with data collected via UAV transects during a controlled release experiment (see Section 2.1). In the UAV flight measurements, the diameter of the source varied between 0.1 and 7.8 cm. To model the methane release from such small emitting surfaces, the spatial resolution needs to be 0.05 - 0.1 cm, following the recommendation from Ardeshiri et al.[30] to have at least 4 pixels in each direction to precisely model the gas release.

The CH_4 plume dynamics were simulated using two distinct FDS configurations to facilitate both detailed analysis and parameter sensitivity testing.
Configuration 1: High-Resolution Nested Grid (Main Study)
This setup was used for the main study and incorporates real terrain topography:

- Domain Size: $162 \times 162 \times 97$ m^3 (shown in Figure 2 (Top)).
- Spatial Resolution (Horizontal): A nested grid was employed, ranging from a fine 4 cm resolution in the center to a coarse 1.08 m at the external boundary. The resolutions used were 4 cm, 12 cm, 48 cm, and 1.08 m.
- Spatial Resolution (Vertical): The vertical resolution was set to twice the horizontal resolution at each grid cell, spanning 97 m. This height is greater than the 50 m maximum altitude

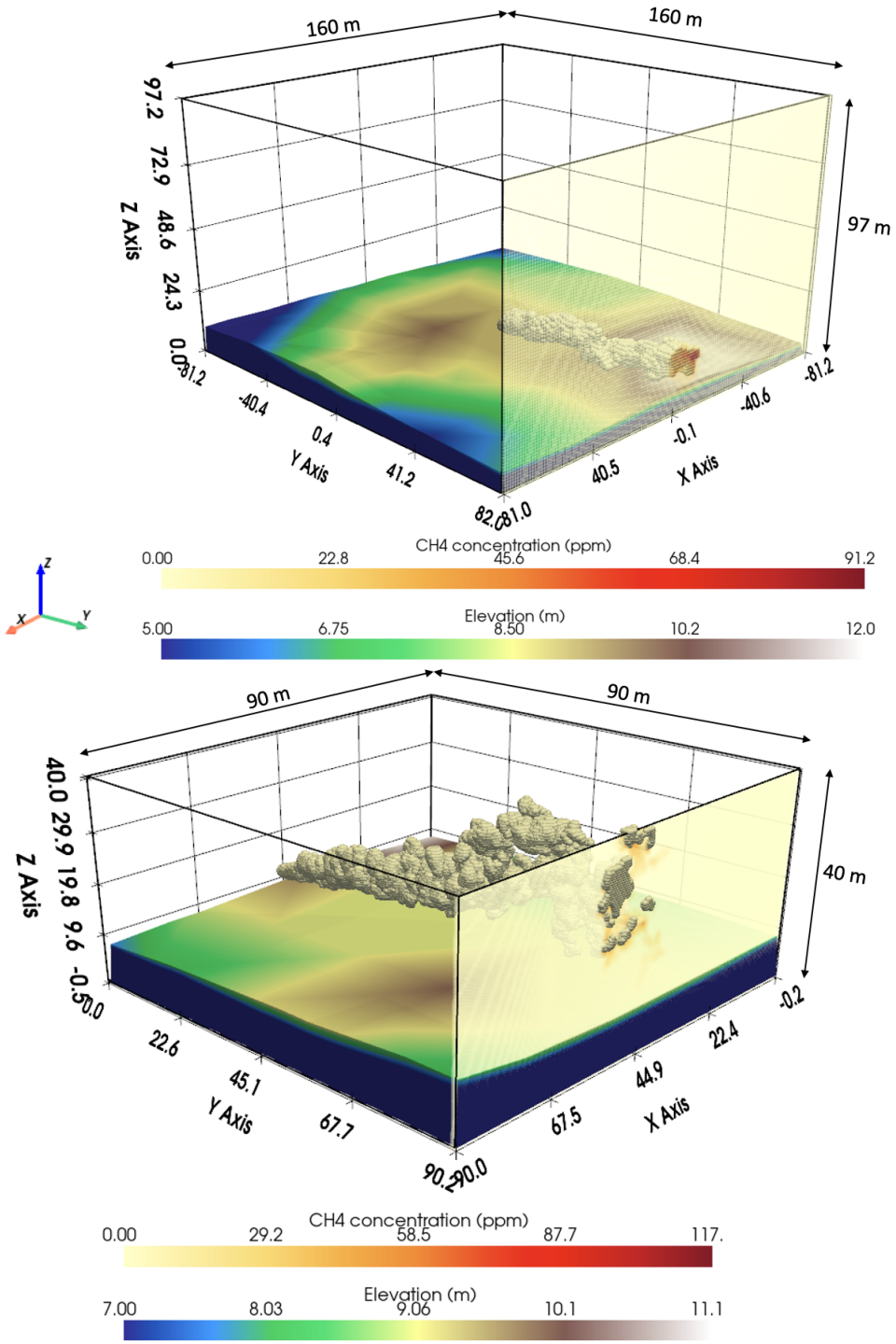

Figure 2: Simulated CH_4 plume shape from FDS domains with the real terrain topography. (Top) The panel shows the corresponding CH_4 concentration enhancement across the plane (opposite lateral boundary). Methane is released from the centre of the domain at 1.5 m above ground (Domain: $162 \times 162 \times 97$ m^3). (Bottom) Methane is released from a lateral boundary via a thin plate (Domain: $90 \times 90 \times 40$ m^3; spatial resolution: 20 cm).

of the UAV transects.

- Computational Cost: The simulation required 104 MPI processes and approximately 27,000 grid points per process, taking nearly 20 hours to simulate 2400 s.

- Release Point: Methane was released from the center of the domain at 1.5 m above ground.

Configuration 2: Uniform Resolution Grid (Sensitivity Test)
A second, smaller configuration was used to test the sensitivity of parameters such as gas release height and temperature:

- Domain Size: $90 \times 90 \times 40$ m^3.
- Spatial Resolution: A constant resolution of 20 cm was used throughout the entire domain in both horizontal and vertical directions.
- Source Design: To utilize the full domain for the study and eliminate obstacle effects, the source was designed as a thin plate placed at the downstream end of the lateral boundary at 1.5 m above ground (as shown in Figure 2 (Bottom)).
- Computational Cost: This configuration required 225 MPI processes and 90,000 grid points per process, also taking nearly 20 hours of real-time to simulate 2400 s.

For the 4 cm spatial resolution and a source of 16×16 cm^2 (*cf.* Supporting Information S2), the exit velocity is held constant between the observed data and the FDS constant. If the exit velocity is constant, the mass flux would multiply as much as the ratio of the original source to the FDS source area. Thus, the area ratio between the observed source and the FDS source is computed, which in turn helps to calculate the source Flux ratio. In FDS, the source rate is dictated by the source flux (given in Table 1), instead of the real source rate. The final results are then normalised by the area ratio to ensure the exit velocity and concentration of CH_4 are the same in both the UAV measurement campaign and FDS.

Among the ten flights used for model evaluation, five of them correspond to releases from pipes that are less than 0.6 cm. For the present configuration, the ratio of source size between the modelled release and the actual pipe diameter varied between 5.36 and 14486.63 (given by Area ratio in Table 1). We discuss later potential avenues to solve the jet representation problem without coupling our FDS simulations to an external jet model.

For the UAV campaign, LiDAR measurements sampled the vertical velocity field at regular intervals, and its time average is given as input to FDS. The unavailable parameters during the measurement campaign, such as ground temperature and ambient air temperature, were downloaded from the ERA5 datasets. Unless specified otherwise, the default value of air pressure used throughout the present work is 101.32 kPa, and the default value of air temperature is 20 °C. The terrain topography was obtained from the Shuttle Radar Topography Mission (SRTM1) datasets of NASA[31] with a spatial resolution of 30 m. This SRTM1 dataset is interpolated (spline) to the appropriate resolution and added to the FDS input file.

Although the UAV flight campaign had measurements between 600 and 4380 s, the UAV flight measurements used in this study lasted between 780 and 1080 seconds. Thus, for each flight from the UAV, FDS is run for approximately 2400 s, where the first 500 seconds are used for spin-up, and the subsequent 1900 seconds of the simulations are used to obtain statistics. The lateral boundary conditions were set to a periodic flow.

Source diameter range	Experiment no	Source diameter (cm)	Source rate (kg_{CH_4} s^{-1})	Area ratio	Source Flux (kg_{CH_4} m^{-2} s^{-1})
Large	0	2.6	0.0095	45.83	17.83
Large	2	7.7	0.03	5.36	6.28
Large	4	0.6	0.001	905.41	35.36
Large	26	0.6	0.002	905.41	70.73
Large	55	0.8	0.005	509.29	99.47
Medium	5	0.27	0.005	4471.18	87.32
Small	22	0.15	0.005	14486.63	282.94
Small	54	0.4	0.001	12732.39	397.88
Medium	60	0.27	0.0005	4471.18	87.32
Medium	63	0.4	0.001	2037.18	79.57

Table 1: Description of the source characteristics for the selected controlled release experiments, including the area ratio and the source flux ratio, both relative to the simulated source area of 16 × 16 cm^2. Source diameter range: Large (> 0.6 cm), Medium (0.4 - 0.6 cm), and Small (< 0.4 cm).

3 Results

3.1 Model evaluation and spatio-temporal variability of plumes

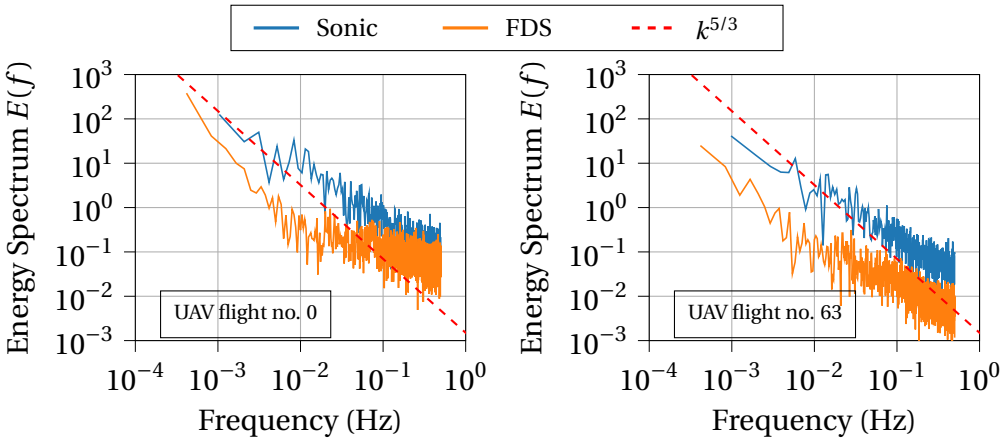

Figure 3: Turbulence Kinetic Energy (TKE) Spectra comparison between FDS simulations and ground-based Sonic anemometer measurements. The data from the Sonic anemometer and FDS simulations correspond to the time periods of two specific UAV flight measurements: 0 and 63.

We validate the simulated turbulence by comparing the 3D velocity field from FDS with measurements from a Sonic anemometer (Sonic instrument). Figure 3 shows the Turbulence Kinetic Energy (TKE) spectrum at a single point, comparing the FDS results (from two of the eight flights used in the current study), with the Sonic datasets at 1 Hz. The TKE from both simulations matches

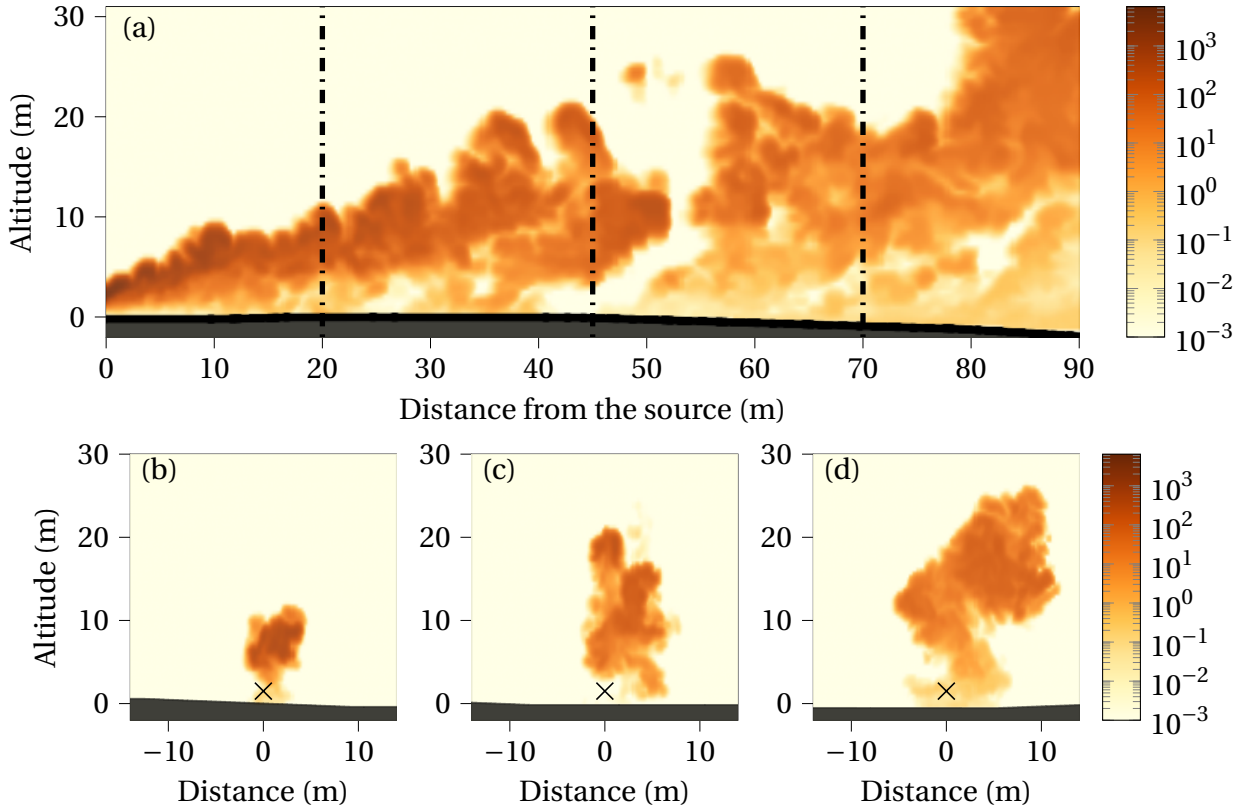

Figure 4: (a) Side view of the instantaneous methane plume. (b-d) Front views of the instantaneous methane plume at downwind distances of 20 m, 45 m, and 70 m from the source. The source is located at (0,1.5) in the coordinate system. The cross symbol (×) in panels (b-d) indicates the altitude of the CH_4 source. The colorbar shows the enhanced methane concentration (ΔCH_4) in ppm.

the observed turbulence spectrum, although the middle range (known as the inertial range) from FDS does not entirely follow that of Sonic. However, this discrepancy is not a model failure; instead, it highlights the need for higher-fidelity terrain, a condition we address in detail in Figure 9. Additional TKE spectra for the remaining UAV flights used in this evaluation are presented in Supporting Information S3.

Figure 4 (a) shows the side view (along the main wind direction) of the instantaneous plume at 2,200 s after the start of the simulation. The plume diffuses proportionally to distance from the source. The simulated enhanced CH_4 concentrations reveal plume dynamics that are primarily driven by buoyancy, the vertical velocity of the released gas, and the horizontal velocity of freestream air. Figure 4 (b-d) shows instantaneous plumes at distances of 20 m, 45 m, and 70 m from the source, corresponding to the range of sampling distances during the UAV measurement campaign. The three instantaneous plume cross-sections (across wind) show the rapid diffusion (both horizontal and vertical) of the CH_4 plume proportional to the distance from the source. These planes show the degree of randomness in the plume shape. The plume is less than 5 m wide (25 m away from the source) to more than 10 m wide (at 70 m from the source). This finding highlights the challenges associated with sampling these plumes using instruments mounted on UAVs. More detailed information regarding the limitations of the UAV sampling methodology is

provided in Supporting Information S4.

3.2 Evaluation of simulated CH_4 plumes from FDS

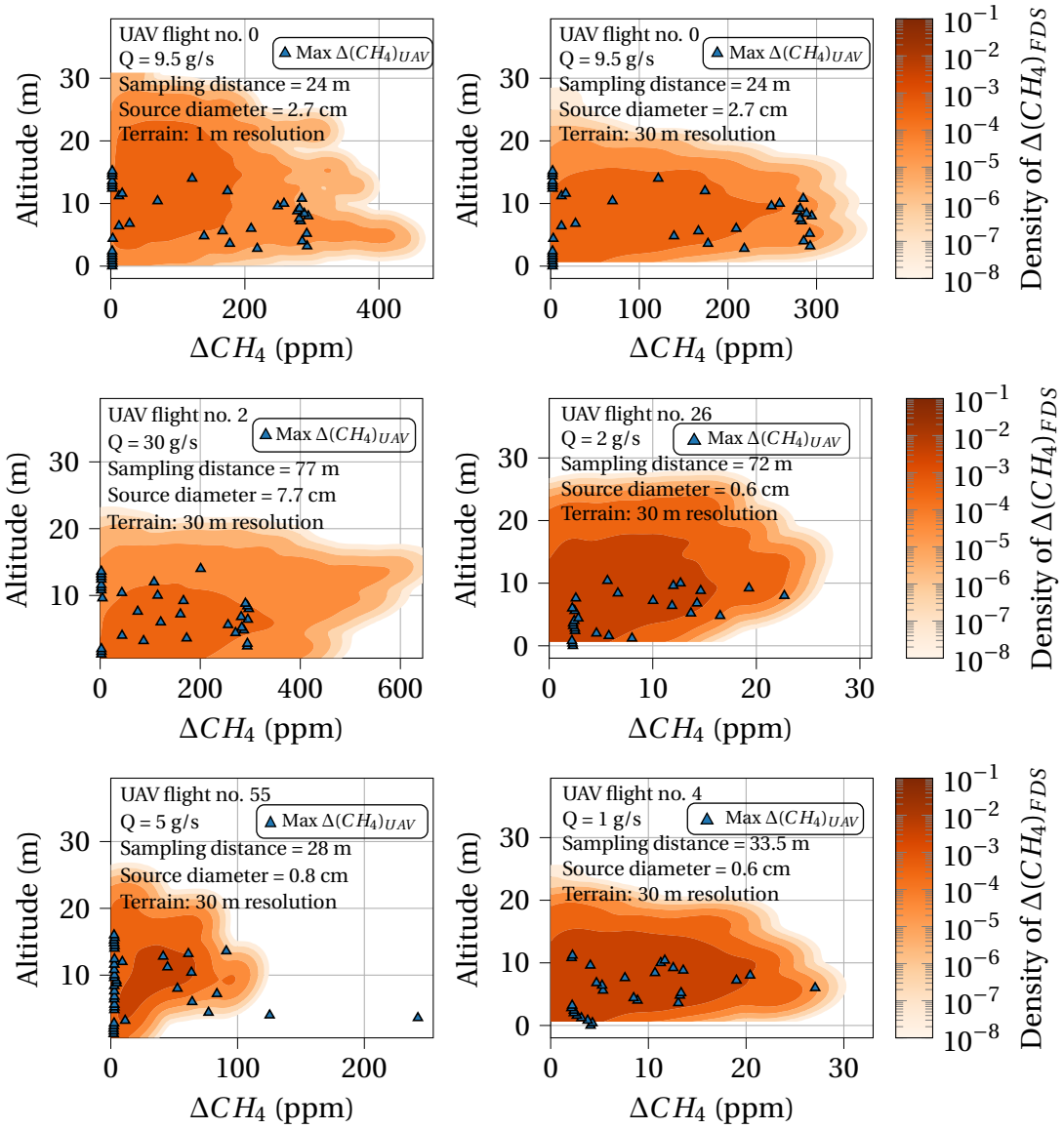

Figure 5: Density of enhanced CH_4 concentration values (in ppm) obtained from sampling FDS results over time (in red) compared to the maximum CH_4 enhancements at each altitude (over time and space) sampled by UAV (denoted as Max $\Delta(CH_4)_{UAV}$ with blue triangles) for 5 flights of the controlled release experiment. The top two panels show the comparison of the UAV flight no. 0, utilising high-resolution 1 m terrain data (left) versus 30 m resolution terrain data (right).

To statistically compare UAV measurement and the FDS simulations, we sample the UAV flight plane in FDS multiple times with the same velocity of the UAV. According to the UAV flight's times at a specific distance from the source, we used the same sampling time (of the order of 600 seconds) to sample all the points at the same distance from the source. We repeated this experiment with a time gap of 100 s, *i.e.*, 500-1100 s, 600-1200 s, and so forth, until 2400 s.

Figure 5 shows the probability of methane concentration value at each altitude as a density map for each time interval (500-1100 s, 600-1200 s, *etc*) compared to the maximum values sampled during the UAV transects obtained over all time and horizontal distances at each altitude (denoted as Max $\Delta(CH_4)_{UAV}$ with blue triangles). We statistically evaluate the plume dimensions and positions in our model simulations. This approach mitigates the undersampling errors from the UAV flights while comparing CH_4 concentration peaks.

For all the flights involving large pipe diameters (> 0.6 cm), the instrumented UAV successfully sampled the plume, with the measured concentrations corresponding well to the most probable values predicted by our FDS simulations. During flight #55, a large peak sampled near the ground by the UAV was never observed in FDS. We believe that these peaks are one of those rare events that occur at the tail end of the PDF, and the simulation may have to run for longer to catch it. Otherwise, the observed enhancements correspond to the envelope of the FDS simulated enhancements. At most altitudes, the observed CH_4 values remain lower than the simulated values. The UAV only sampled one instance of the whole stochastic plume, whereas the FDS results correspond to the plume statistics sampled multiple times.

The sensitivity of these simulations to the underlying topographical data is further demonstrated in flight no. 0, which compares the use of high-resolution (1 m) terrain against SRTM1 (30 m) resolution terrain, is shown in the top two panels of Figure 5. When the 1 m resolution terrain is employed, the resulting plume envelope is notably larger, exhibiting a higher peak and increased plume depth compared to the simulation using the 30 m resolution terrain. This suggests that finer topographical features significantly influence the simulated dispersion characteristics and the resulting plume geometry.

Flight #		0	0†	2	4	26	55	5*	22*	60	63
Height range (m)	Obs	0-15.2	0-15.2	0-14	0-11.3	0-10.5	0-16	0-14.5	0-12.5	0-9.5	0-10
	FDS	0.5-28.5	0-31	0-23.3	0.5-25.5	0.5-28	0-27	0.5-23.5	0.5-22.5	0.5-25	0.5-30
Plume depth (m)	Obs	15.2	15.2	14	11.3	10.5	16	14.5	12.5	9.5	10
	FDS	28	31	23.3	25	27.5	27	23	22	24.5	29.5
Peak value (ppmv)	Obs	294.5	294.5	297	27	24	242.3‡	27.5	18.7	60	88
	FDS	357	470	673	30.3	27.5	125	24	29.5	25.5	34

Table 2: Assessment of plume spatial characteristics comparing FDS simulations to UAV measurements across 9 selected flights. Parameters include vertical extent (height range), CH_4 plume depth, and maximum concentration. Asteriks (*) denote flights adjusted for smaller pipe diameters. The dagger (†) indicates the heatmap for UAV flights no. 0, which utilised high-resolution (1 m) LiDAR datasets; all other simulations utilised 30 m resolution SRTM1 terrain. The double dagger (‡) highlights a peak Δ CH_4 value in Flight #55 that occurred near ground level, falling significantly outside the FDS-calculated density envelope.

Table 2 presents different spatial metrics to evaluate our FDS simulated plumes for all the various flights. Here, the plume depth is the vertical extent of the plume derived from the difference between the maximum and minimum height of the plume. The peak value corresponds to the

absolute maximum value in both UAV flights and their corresponding FDS plume. The FDS plume characteristics agree with the observed enhancements for five of the ten flights. The double dagger symbol (‡) indicates that a peak concentration value from Flight #55 occurred close to the ground, which was significantly outside the range of ΔCH_4 generated by FDS at that altitude. Apart from this peak value, the next highest value from that UAV flight is 125 ppm, which agrees with FDS. For release experiments utilising a small pipe diameter (diameter < 0.6 cm), the modelled source area within FDS is significantly larger (area source ratio > 905.41) than the actual physical source due to grid constraints. To account for non-linear jet heights and produce more realistic plumes for Flights 5 and 22, we manually increased the simulated pipe diameter to 0.6 cm. This action reduced the exit velocity of the CH_4 and resulted in FDS plumes agreeing with UAV flight measurements. For the three remaining flights (54, 60, and 63), our simulated jets remained too high, producing unrealistic plumes (higher and more diffuse than observed). More details on these remaining five flights are given in Supporting Information S5.

3.3 Sensitivity of CH_4 plume structures to external conditions

Following the validation presented in Section 3.2, which compared FDS results with controlled-release datasets, we realised that multiple parameters influence the plume dynamics. Therefore, this subsection focuses on a sensitivity analysis of the critical factors—the height of release, exit velocity, terrain topography, obstacles, and the CH_4 release temperature—on the plume dynamics as it is transported by the turbulent atmospheric flow.

3.3.1 Influence of exit velocity

The exit velocity of the gas release is a crucial parameter, as it primarily determines the plume's trajectory and its effective velocity within the constant ambient flow. For instance, a slow release from a large source and a fast release from a small source may have the same mass flow rate, but produce vastly different plumes in terms of the vertical and horizontal distributions. Therefore, the plume's effective velocity—which is intrinsically linked to the vertical distribution—varies proportionally with the exit velocity, even if the ambient wind speed remains unchanged.

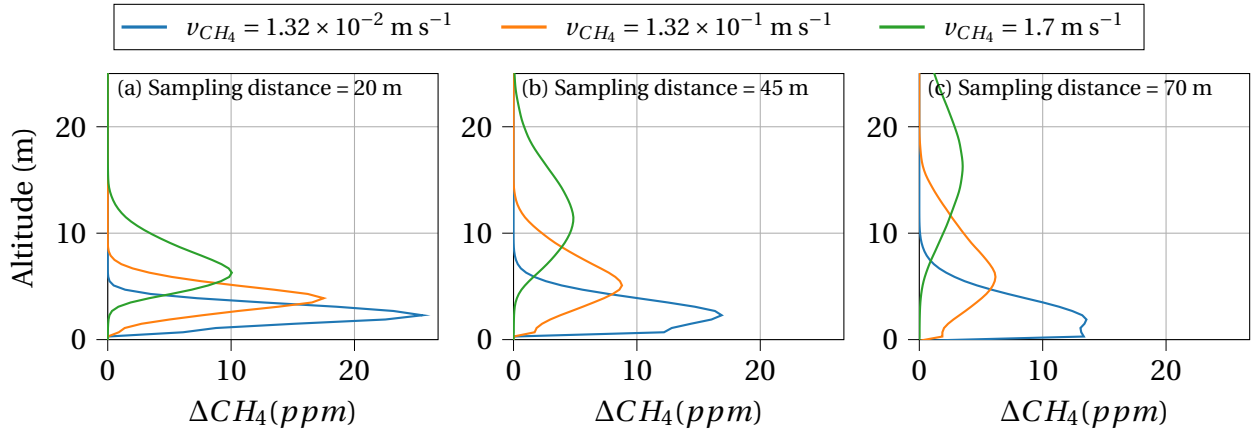

Figure 6: Averaged vertical distribution of modelled CH_4 concentration enhancements as a function of source exit velocities and downwind distances from the source.

Figure 6 displays the vertical distribution of CH_4 concentration enhancement (averaged horizon-

tally) across different vertical exit velocities, for a constant mass flow rate of 9.5 g_{CH_4} s^{-1}. To obtain these profiles, the mass flow rate was increased by a certain factor, and the resulting CH_4 concentration was then normalised by that same factor. Specifically, the normalisation factor was 1 for 1.3×10^{-2} m s^{-1}, 10 for 1.3×10^{-1} m s^{-1}, 127 for 1.7 m s^{-1}. We show that the exit velocity directly determines the height at which the plume is released into the atmosphere.

- The highest exit velocity (1.7 m s^{-1}) injects the plume highest and causes it to rise faster in the atmosphere and diffuse most rapidly.
- The lowest exit velocity (1.3×10^{-2} m s^{-1}) results in the CH_4 plumes trapped in the viscous surface layer of the Atmospheric Boundary Layer, remaining near the ground even at 70 m away from the source.
- The intermediate exit velocity (1.3×10^{-1} m s^{-1}) plume diffuses upward but more slowly than the highest exit velocity case.

We investigated varying CH_4 release heights to determine if the influence of gas exit velocity is solely attributable to initial plume height near the source. Our results indicate that simply increasing the release height does not appreciably alter vertical diffusion. Instead, the behaviour observed in Figure 6 is linked to increased plume turbulence—proportional to the exit velocity—rather than the release altitude itself (*cf.* Supporting Information S6). We therefore conclude that for sources located up to 5 m a.g.l., the initial height of release is a secondary factor in the overall CH_4 vertical distribution. It is important to note that these findings pertain to low-level release typical of ground-based or UAV-scale assessments; the dynamics may differ significantly for emissions from industrial stack towers exceeding 100 m, which are beyond the scope of this study. Furthermore, we show that plume diffusion and height as a function of distance remain non-linear for the three CH_4 exit velocities considered here, up to 70 m from the source.

3.3.2 Influence of terrain topography

We investigate here the impact of the topography on the spatial distribution of the atmospheric CH_4 enhancements. The terrain topography information from SRTM1 (30 m spatial resolution) is interpolated to the simulation's spatial resolution to prevent the introduction of artificial obstacles.

Figure 7 illustrates the strong influence of terrain topography on both the CH_4 plume height and its vertical extent, an effect that is highly dependent on the gas exit velocity. For accurate comparison, all vertical levels in the terrain cases are referenced to Above Ground Level (AGL) using a terrain-following coordinate system.

The results demonstrate a clear velocity-dependent impact:

- Low Exit Velocity Case: At 1.3×10^{-2} m s^{-1}, the 30 m resolution terrain has a minimal effect on plume dynamics, with the concentration field remaining continuous and largely unaffected even 90 m downwind.
- High Exit Velocity Case: Conversely, at 1.7 m s^{-1}, the 30 m terrain information significantly impacts the CH_4 plume, causing a difference of approximately 10 m in the plume's altitude 80 m from the source.

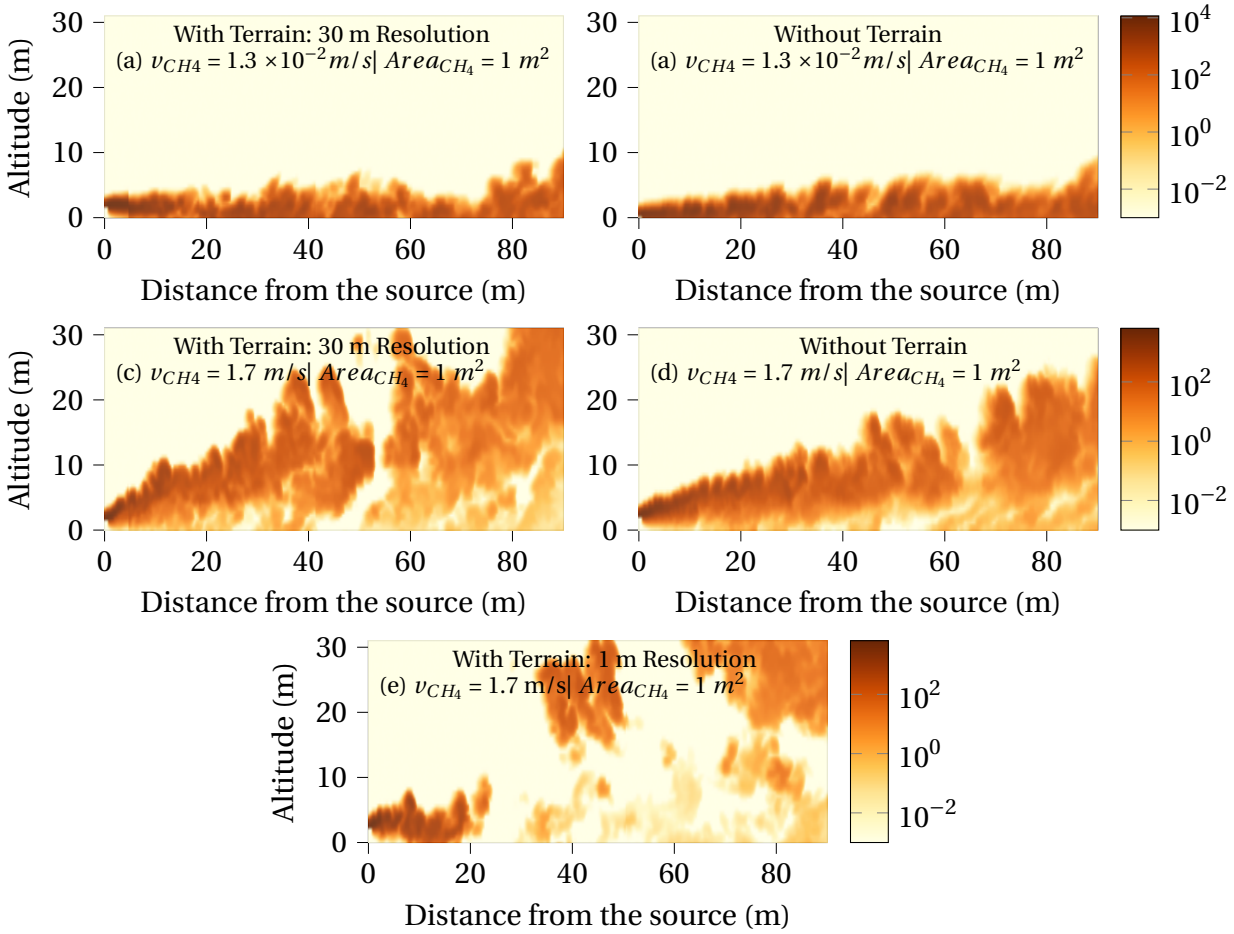

Figure 7: Instantaneous simulated atmospheric CH_4 enhancements are presented in ppm. The left column shows the simulation with terrain topography (terrain-following coordinates), and the right column shows the simulation without terrain topography. The top row uses a low exit velocity (1.3 x 10^{-2} m s^{-1}), while the middle row uses a high exit velocity (1.7 m s^{-1}). The bottom-centre panel is the same as (c), except with terrain topography using 1 m resolution terrain data. All simulations have the methane source located at 1.5 m above ground level.

When the exit velocity of the plume is low, it stays near the ground for a long distance where the free stream wind speed is extremely low. These plumes almost never interact with the turbulent air present away from the ground; even if the terrain complexities create a turbulent flow, the low-speed CH_4 remains in the viscous sublayer, which is barely turbulent. In contrast, a high-speed CH_4 release escapes the viscous sublayer and is injected into the high-speed turbulent air at higher altitudes. Consequently, the trajectory of a high-speed plume becomes highly dependent on terrain topological features, as the release is directly subjected to the turbulence and flow patterns generated by the complex terrain.

The inclusion of the high-resolution 1 m terrain data (shown in the bottom central panel) reveals a distinctly different plume structure. Unlike the continuous plumes observed with the 30 m resolution, the 1 m simulation shows the plume becoming highly turbulent and discontinuous. This finding confirms that flow dynamics are strongly influenced by small-scale obstacles (less than 30

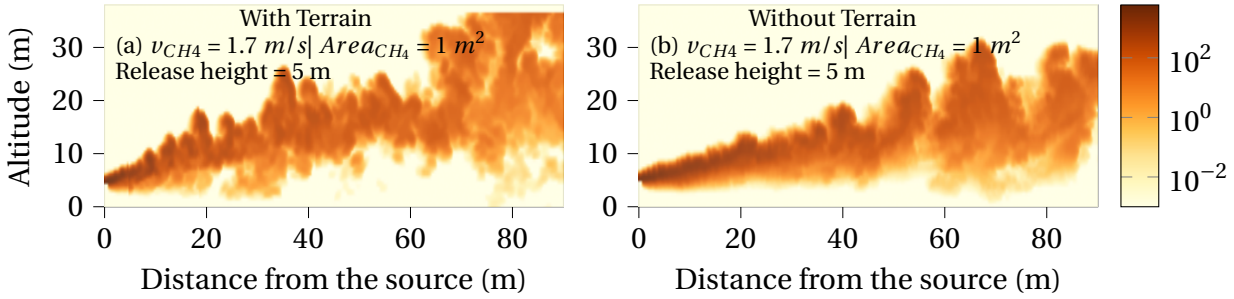

Figure 8: Instantaneous simulated atmospheric CH_4 enhancements from a source located at 5 m above ground level (AGL). The left panel shows the simulation with terrain topography (using a terrain-following coordinate system), while the right panel shows the simulation without terrain topography. The colorbar indicates the enhanced methane concentration (Δ CH_4) in ppm.

m resolution) present in the high-resolution data. Collectively, these findings suggest that terrain influence is primarily governed by the gas exit velocity, making the use of high-resolution terrain essential for capturing the precise, turbulent characteristics of high-velocity point source plumes.

Figure 8 shows the influence of terrain topography on the simulated atmospheric CH_4 enhancements with a source located at 5 m above ground level. At such release heights, both plumes (with and without terrain topology information) remain several meters above the ground. Yet the differences in vertical diffusion (and in turn plume height) between with and without terrain are as profound as the counterparts in Figure 7. The time-averaged plume also exhibits the same pattern of differences observed in the instantaneous results; a full analysis of these sustained characteristics is presented in Supporting Information S7. We examined the Turbulent Kinetic Energy (TKE) spectrum to quantify the terrain topography influence on the turbulence scales.

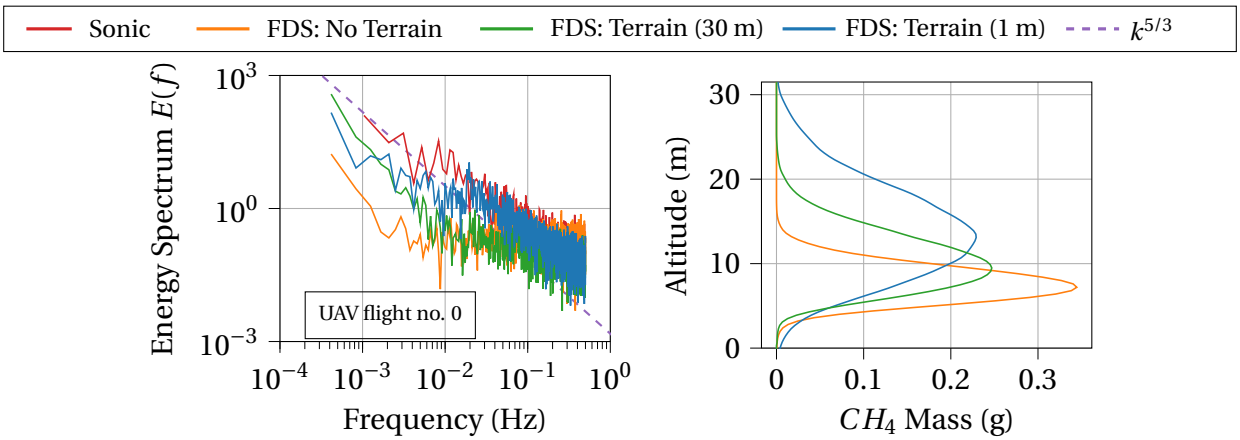

Figure 9: Comparison of simulated and measured atmospheric quantities during UAV Flight No. 0. The left panel shows the Turbulent Kinetic Energy (TKE) spectra from FDS simulations compared to ground-based Sonic anemometer measurements. The right panel shows the time-averaged vertical profile of the total CH_4 mass concentration at 35 m downwind from the source. Both plots include results for three FDS simulation cases: with 1 m resolution terrain, with 30 m resolution terrain, and without terrain topography.

Figure 9 illustrates the substantial influence of terrain topography resolution on atmospheric dy-

namics and plume dispersion, presenting the Turbulent Kinetic Energy (TKE) spectra (left) and the time-averaged vertical CH_4 mass profile (right) from FDS simulations, compared against Sonic anemometer measurements during UAV flight #0. Analysis of the TKE spectra shows that the high-resolution 1 m terrain is essential; it is the only case that fully establishes the expected inertial range (with the -5/3 slope) and closely matches the Sonic instrument's spectrum across most frequencies. This turbulence is reflected in the vertical plume structure, where the average vertical diffusion and plume height are highest in the 1 m terrain case. While the no-terrain case completely lacks an inertial range, the 30 m resolution terrain still reasonably recreates the TKE at small (low) frequencies and captures the general upward shift in plume height and diffusion shown in the vertical profiles. However, the 30 m resolution fails to capture the turbulence in the inertial and high-frequency ranges. We conclude that using the 1 m resolution terrain is critical for accurately simulating the full spectrum of turbulence and resulting plume characteristics; however, in its absence, 30 m terrain data provides a foundation for approximating TKE at larger scales and capturing general plume trends.

3.3.3 Influence of obstacles

Obstacles present in the domain can significantly impact the CH_4 plume dynamics, with the effect depending on the mean wind direction and the obstacles' geometry. We investigated the potential impact of large cylinders, simulating structures such as pressure tanks in oil and gas fields or large mine stacks (*e.g.,* coal mine shafts). To examine this situation, the methane source was simulated on a 1 m^2 cylinder placed 5 m above ground level (*cf.* Figure 10).

The obstacle's presence (cylinder) generates wake vortices when air passes over it, which influences the methane plume dynamics just downstream of the obstacle. This downward airflow naturally directs the methane towards the ground, despite the fact that methane typically rises due to its buoyancy.

To test the hypothesis that wind influences the methane's downward movement, simulations were conducted using wind speed reduced to 25 % of the original value (U_{10m}= 3.3 m s^{-1}), as shown in Figure 10. The results reveal that as wind speed decreases, the plume is less constrained by the wind force, allowing methane to rise to higher altitudes from the source due to buoyancy. Conversely, at higher wind speeds, the flow becomes more turbulent, causing the methane to be more influenced by aerodynamic forces around obstacles. We conclude here that the obstacles——like tanks, buildings, forests, or storage piles——can significantly alter the flow dynamics of the methane plume at short distances (< 50 m away from the source), depending on the complexity of the environment.

3.3.4 Influence of exit temperature

Regarding the nature of the potential CH_4 sources across the globe, two main types of sources are detected and measured: passive sources from diffusion into the atmosphere (*e.g.,* manure, open landfills, rice paddies, wetlands) and pressurised leaks (*e.g.,* compressor stations, storage tanks, gas lines). Hence, CH_4 molecules are being released at low temperatures (due to adiabatic decompression of the gas - Joule-Thomson effect) and high temperatures (from exothermic decomposition, such as in the case of landfills) compared to ambient air. Depending on the temperature difference (both sign and amplitude), the gas could either rise or descend once released. To test the influence of temperature on the CH_4 plume dynamics, we simulated 4 scenarios using FDS with

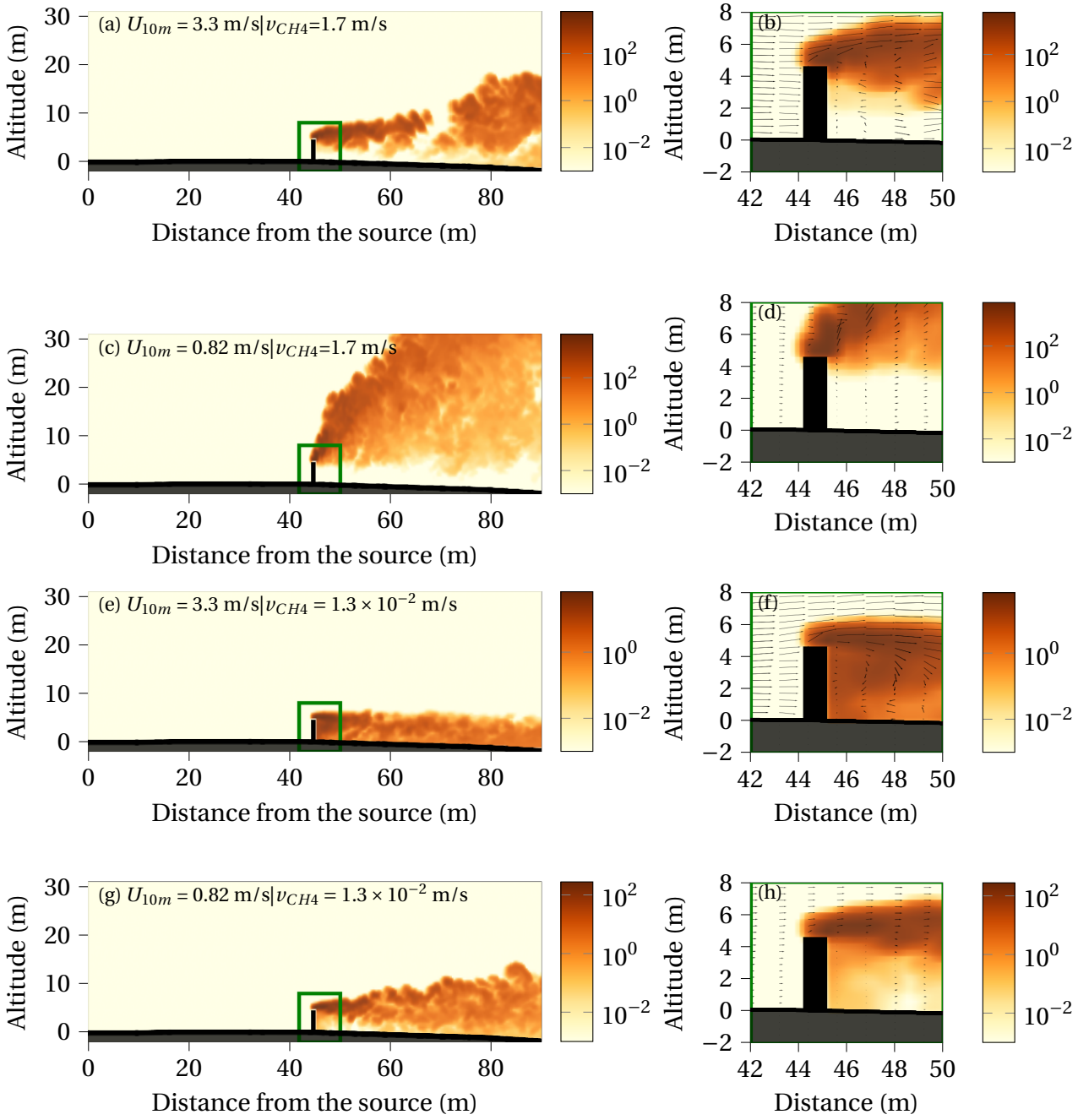

Figure 10: Vertical plane of the simulated instantaneous atmospheric CH_4 enhancements (along wind) originating from the top of an obstacle (cylinder) at 5 m above the ground, with free stream velocity at 10 m U_{10m}= 0.82 m s^{-1} (a-b and e-f) and U_{10m} = 3.3 m s^{-1} (c-d and g-h). Exit velocity U_{CH_4} =1.3 × 10^{-2} m s^{-1} for (a-d), U_{CH_4} = 1.7 m s^{-1} for (e-h). The right column shows a zoomed view of the plume to describe the obstacle impact at short distances. The colorbar shows the enhanced methane concentration (Δ CH_4) in ppm.

high-speed (1.7 m s^{-1}) and low-speed (1.3 × 10^{-2} m s^{-1}) methane exit velocity, high-temperature (80 °C - thermophilic anaerobic digestion) and low temperature (-80 °C - rapid decompression during blowdowns). We normalised appropriately to keep the mass flow rate constant in all simu-

lations.

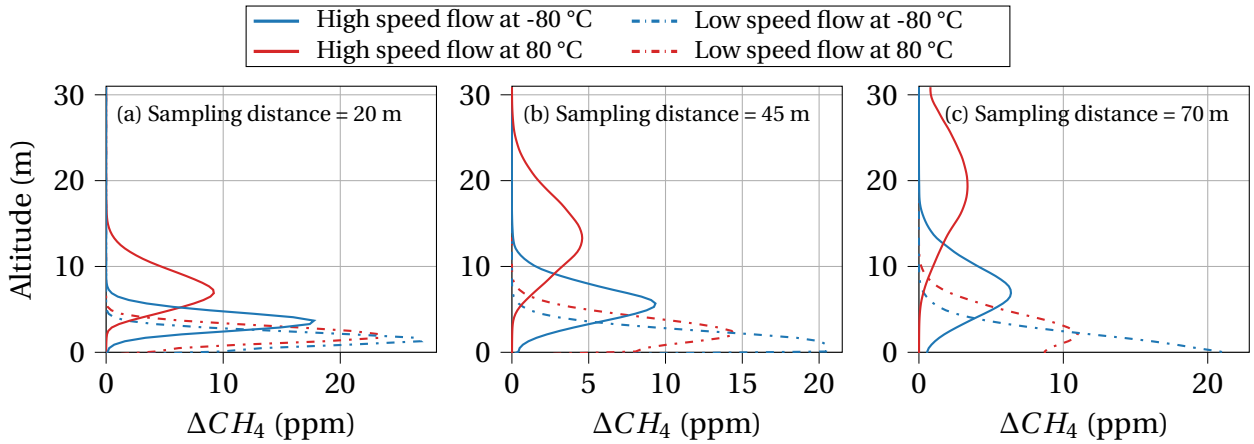

Figure 11: Vertical distribution of CH_4 enhancements (in ppmv) as a function of the gas temperature (-80 °C and +80 °C) at 20m, 45m, and 70m from the source, averaged over space and time, using a high exit velocity (1.7 m s^{-1}) and a low exit velocity (1.3 × 10-2 m s^{-1}).

Figure 11 shows the vertical distribution of the CH_4 plume coming out at two different velocities (1.7 m s^{-1} and 1.3 × 10^{-2} m s^{-1}) and two different temperatures (-80 °C and +80 °C) at various distances from the source. As expected, the high exit velocity generates a CH_4 plume at higher altitudes compared to the low exit velocity ones. Regarding the gas temperature, the high-temperature gas source produces a plume rising at higher altitudes faster than the low-temperature case. We note that the plume expands rapidly up to 30 m away from the source. We examine the rise of the plume by comparing the motion of the warm and cold releases to the original case (gas released at air temperature) in Figure 12.

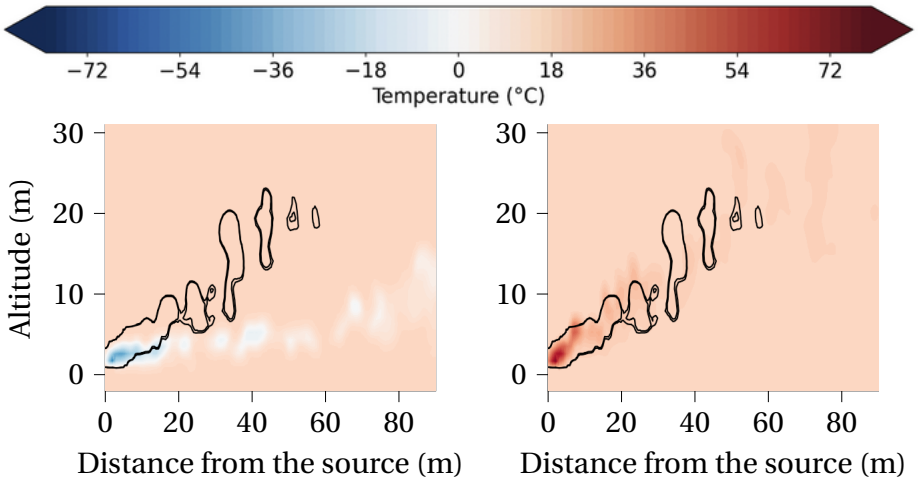

Figure 12: Temperature profiles (in °C) of the methane released at 80 °C (left panel) and -80 °C (right panel), and CH_4 enhancement contour lines (300 ppm) delineating the plume extent in black from the original release case (ambient gas temperature). The velocity of release is 1.7 m s^{-1}.

Despite having the same exit velocity, the temperature anomaly decreases rapidly in the first 20 m from the source. Both the cold and hot gas releases reach ambient temperature between 10 m and 30 m at an exit velocity of 1.7 m s^{-1}. The temperature anomaly dictates the rapidity at which the plume rises into the atmosphere, with the hot plume rising faster than the cold one. We show that the cold release case has a lower elevation and doesn't match that of ambient temperature up to 35 m, the hot gas release at 80 °C resembles the original simulation at 20 °C (Fig. 12, right panel). Finally, we note that the slow case (exit velocity of 1.3×10^{-2} m s^{-1}, not shown here) generates the same plume as the original simulation. The lower exit velocity rapidly reaches its energetic equilibrium a few meters away from the source. We conclude here for dry gas (pure methane) that only large sources at low temperatures (*e.g.,* compressor blowdowns) will generate significantly different plume elevations and shapes. Future experiments will include warm sources in cold air (*e.g.,* manure lagoon during wintertime) to examine the entire spectrum of gas and air temperatures.

4 Discussion

The comparison of FDS simulated plumes with in-situ measurements from controlled release of methane demonstrates that FDS can achieve a CH_4 concentration enhancement similar in height, depth, and magnitude to the field data. This accurate simulation was consistently effective only when the ratio of the simulated to the real source diameter was less than or equal to 26.67 (corresponding to a real source diameter of 0.6 cm and a simulated source diameter of 16 cm). For real source diameters with a ratio greater than this threshold——specifically, for real source diameters smaller than 0.6 cm in the current study——we adjusted the source diameter to 0.6 cm. This adjustment method was effective for only two out of the five UAV flights, with no clear explanation for its selective success. Based on these results, we conclude that accurately modelling CH_4 plumes with FDS requires the diameter ratio to be less than or equal to 26.67.

The simulated methane plume dynamics demonstrate that the influence of each parameter is highly dependent on the gas exit velocity. Although these sensitivity results pertain to a specific location, we postulate that the effects of gas temperature, obstacles, and exit velocity would be similar across different sites. Our findings, ranked by order of importance, are summarised in Table 3.

The terrain topography emerges as the main factor governing the plume shape, with its influence remaining significant even at 40 m from the source. This effect is most prominent when the methane exit velocity reaches 1.7 m s^{-1}. We established the superiority of using a 1 m resolution terrain topography, which generates a TKE spectrum that closely matches the observation. Failing to obtain a 1 m resolution, 30 m resolution terrain topography remains important as it still captures the general plume trends and approximates the TKE spectrum of Sonic at some scales, which is much better than the simulation without any terrain topography.

Furthermore, our obstacle results suggest that a higher free-stream air velocity would impact the plume to a greater degree than a lower free-stream air velocity, in the presence of terrain. Crucially, the influence of obstacles is most pronounced in the vertical direction: the vortices created around the obstacle by the air flowing over it tend to push the plume downwards. The intensity of this downward push is proportional to the air velocity. We expect this effect wherever the plume traverses solid structures such as tall buildings or any other obstacles in its path. We also show that the higher the velocity of release, the more energetic the plume becomes, leading to more rapid

diffusion and atmospheric rise.

The gas release temperature is a significant parameter for high, cold gas exit velocities (1.7 m s^{-1} and -80 °C, respectively), up to a certain distance from the source. Specifically, the plume reaches ambient air temperature within 35 m from the source when released at 1.7 m s^{-1}, but within only a few meters when released at 1.3×10^{-2} m s^{-1}. Although the difference in plume heights near the source is minimal (< 5 m), plumes at different temperatures become substantially divergent at 70 m from the source, even when sharing the same exit velocity. Conversely, the gas release height, varying from 1.5 m to 5 m, remains a secondary parameter in plume dynamics.

Parameter	Degree of Influence	
	high velocity	Low velocity
Terrain Topography	High	Low
Temperature of release (-80 °C/ +80 °C)	Medium/High	Medium/Low
Velocity of air	High	Low
Height of release	Low	Low
Obstacle (Low wind speed : 0.82 m s^{-1})	Low	Low
Obstacle (High wind speed : 3.33 m s^{-1})	High	Medium

Table 3: Degree of influence (relative importance) of the various external and internal parameters used in FDS simulations on the spatial distribution of the simulated atmospheric CH_4 enhancements.

The present work proves that Large Eddy Simulations (LES) can accurately reproduce observed CH_4 plumes from a controlled release experiment, provided the model is constrained by in-situ wind measurements, actual terrain, source exit velocity, and the source diameter. While FDS successfully simulates plumes from sufficiently large pipes (> 0.6 cm diameter), the model inaccurately represents the jet from small tubes (< 0.5 cm), modelling an unrealistically stronger jet at the release location. This limitation stems from the source area being too small relative to the model resolution to accurately capture the jet physics.

The spatial distribution of the CH_4 plume near the source is highly responsive to parameters such as terrain topography, gas exit velocity, gas temperature, and the presence of obstacles along the plume path. Specifically, the effect of the surface layer is visible for the plumes released near the ground at a low velocity (1.3×10^{-2} m s^{-1}), where methane is effectively trapped in the slow-moving air close to the ground over long distances before rising towards the Atmospheric Boundary Layer.

Supporting Information

Fire Dynamics Simulation (FDS) parameters; spectral data for remaining UAV flights; UAV flight evaluation density maps with 0.6 cm diameter adjustments; analysis of release height and terrain topology influences (PDF).

Author information

Corresponding Author
Rakesh Yuvaraj: Université de Reims Champagne-Ardenne, 51100 Reims, France
Email: rakesh.yuvaraj@univ-reims.fr
ORCID: 0009-0005-9666-5983

Notes

A preprint of this research article is available at DOI: 10.26434/chemrxiv-2025-lv32x[32]
The authors declare no competing financial interest.

Abbreviations

The following are the abbreviations used in the present work:
AGL: Above Ground Level
AUSEA: Airborne Ultra-light Spectrometer for Environmental Application
ERA5: ECMWF Reanalysis v5
FDS: Fire Dynamics Simulations
LiDAR: Light Detection And Ranging
LES: Large Eddy Simulations
MPI: Message Passing Interface
PDF: Probability Density Function
SGS: Sub-Grid-Scale
SNR: Signal to Noise Ratio
SRTM: Shuttle Radar Topography Mission
TKE: Turbulence Kinetic Energy
UAV: Uncrewed Aerial Vehicle

Acknowledgements

This work was supported by the European Space Agency (MethaneWatch project), the SIMEA project (BPI Grand Est), and the French Ministry for Research and Education (MESRI, Chaire de Professeur CASAL). The work was granted access to the HPC resources of IDRIS under the allocations 2024-0115628, 2024-0116045, 2025-116134 made by GENCI (Grand Équipement National de Calcul Intensif). The authors would like to thank the access to HPC resources ROMEO, part of Université de Reims Champagne-Ardennes. The authors would like to thank Dr. Pramod Kumar and Dr. Gregoire Broquet for sharing the wind measurements from the Sonic instrument, which helped to compare the turbulence spectra between FDS and observations.

References

[1] Stefanie Kirschke, Philippe Bousquet, Philippe Ciais, Marielle Saunois, Josep G Canadell, Edward J Dlugokencky, Peter Bergamaschi, Daniel Bergmann, Donald R Blake, Lori Bruhwiler,

et al. Three decades of global methane sources and sinks. *Nature geoscience*, 6(10):813–823, 2013.

[2] Thomas Lauvaux, Clément Giron, Matthieu Mazzolini, Alexandre d'Aspremont, Riley Duren, Dan Cusworth, Drew Shindell, and Philippe Ciais. Global assessment of oil and gas methane ultra-emitters. *Science*, 375(6580):557–561, 2022.

[3] Thibaud Ehret, Aurélien De Truchis, Matthieu Mazzolini, Jean-Michel Morel, Alexandre D'aspremont, Thomas Lauvaux, Riley Duren, Daniel Cusworth, and Gabriele Facciolo. Global tracking and quantification of oil and gas methane emissions from recurrent sentinel-2 imagery. *Environmental science & technology*, 56(14):10517–10529, 2022.

[4] James P Williams, Mark Omara, Anthony Himmelberger, Daniel Zavala-Araiza, Katlyn MacKay, Joshua Benmergui, Maryann Sargent, Steven C Wofsy, Steven P Hamburg, and Ritesh Gautam. Small emission sources in aggregate disproportionately account for a large majority of total methane emissions from the us oil and gas sector. *Atmospheric Chemistry and Physics*, 25(3):1513–1532, 2025.

[5] Climate and Clean Air Coalition. Global methane pledge, 2023. URL https://www.globalmethanepledge.org/resources/global-methane-pledge. Accessed: January 21, 2026.

[6] Evan D Sherwin, Jeffrey S Rutherford, Yuanlei Chen, Sam Aminfard, Eric A Kort, Robert B Jackson, and Adam R Brandt. single-blind validation of space-based point-source detection and quantification of onshore methane emissions. *Scientific Reports*, 13(1):3836, 2023.

[7] Luis Guanter, Javier Roger, Shubham Sharma, Adriana Valverde, Itziar Irakulis-Loitxate, Javier Gorroño, Xin Zhang, Berend J Schuit, Joannes D Maasakkers, Ilse Aben, et al. Multisatellite data depicts a record-breaking methane leak from a well blowout. *Environmental Science & Technology Letters*, 11(8):825–830, 2024.

[8] Pramod Kumar, Grégoire Broquet, Camille Yver-Kwok, Olivier Laurent, Susan Gichuki, Christopher Caldow, Ford Cropley, Thomas Lauvaux, Michel Ramonet, Guillaume Berthe, et al. Mobile atmospheric measurements and local-scale inverse estimation of the location and rates of brief ch 4 and co 2 releases from point sources. *Atmospheric measurement techniques*, 14(9):5987–6003, 2021.

[9] Jean-Louis Bonne, Ludovic Donnat, Grégory Albora, Jérémie Burgalat, Nicolas Chauvin, Delphine Combaz, Julien Cousin, Thomas Decarpenterie, Olivier Duclaux, Nicolas Dumelié, et al. A measurement system for co 2 and ch 4 emissions quantification of industrial sites using a new in situ concentration sensor operated on board uncrewed aircraft vehicles. *Atmospheric Measurement Techniques*, 17(14):4471–4491, 2024.

[10] Randulph Morales, Jonas Ravelid, Katarina Vinkovic, Piotr Korbeń, Béla Tuzson, Lukas Emmenegger, Huilin Chen, Martina Schmidt, Sebastian Humbel, and Dominik Brunner. Controlled-release experiment to investigate uncertainties in uav-based emission quantification for methane point sources. *Atmospheric Measurement Techniques*, 15(7):2177–2198, 2022.

[11] Tianran Han, Conghui Xie, Yayong Liu, Yanrong Yang, Yuheng Zhang, Yufei Huang, Xiangyu Gao, Xiaohua Zhang, Fangmin Bao, and Shao-Meng Li. Development of a continuous uav-mounted air sampler and application to the quantification of co 2 and ch 4 emissions from a major coking plant. *Atmospheric Measurement Techniques*, 17(2):677–691, 2024.

[12] Han Yong, Grant Allen, Jamie Mcquilkin, Hugo Ricketts, and Jacob T Shaw. Lessons learned from a uav survey and methane emissions calculation at a uk landfill. *Waste Management*, 180:47–54, 2024.

[13] Jonathan F Dooley, Kenneth Minschwaner, Manvendra K Dubey, Sahar H El Abbadi, Evan D Sherwin, Aaron G Meyer, Emily Follansbee, and James E Lee. A new technique for airborne measurements to quantify methane emissions over a wide range: Implementation and validation. *EGUsphere*, 2024:1–26, 2024.

[14] Xiao-Ming Hu, Wesley T Honeycutt, Chenghao Wang, Binbin Weng, Bowen Zhou, and Ming Xue. Observation and simulation of methane plumes during the morning boundary layer transition. *Journal of Geophysical Research: Atmospheres*, 130(7):e2024JD042317, 2025.

[15] JOEL H Ferziger. Subgrid-scale modeling. *Large eddy simulation of complex engineering and geophysical flows*, 37:54, 1993.

[16] Robert D Moser, Sigfried W Haering, and Gopal R Yalla. Statistical properties of subgrid-scale turbulence models. *Annual Review of Fluid Mechanics*, 53(1):255–286, 2021.

[17] Daniel J Varon, J McKeever, D Jervis, JD Maasakkers, Sudhanshu Pandey, S Houweling, I Aben, T Scarpelli, and DJ Jacob. Satellite discovery of anomalously large methane point sources from oil/gas production. *Geophysical Research Letters*, 46(22):13507–13516, 2019.

[18] Mark Omara, Daniel Zavala-Araiza, David R Lyon, Benjamin Hmiel, Katherine A Roberts, and Steven P Hamburg. Methane emissions from us low production oil and natural gas well sites. *Nature Communications*, 13(1):2085, 2022.

[19] Anders Nottrott, Jan Kleissl, and Ralph Keeling. Modeling passive scalar dispersion in the atmospheric boundary layer with wrf large-eddy simulation. *Atmospheric environment*, 82: 172–182, 2014.

[20] Camille Viatte, Thomas Lauvaux, Jacob K Hedelius, Harrison Parker, Jia Chen, Taylor Jones, Jonathan E Franklin, Aijun J Deng, Brian Gaudet, Kristal Verhulst, et al. Methane emissions from dairies in the los angeles basin. *Atmospheric Chemistry and Physics*, 17(12):7509–7528, 2017.

[21] Anja Ražnjević, Chiel Van Heerwaarden, Bart Van Stratum, Arjan Hensen, Ilona Velzeboer, Pim Van Den Bulk, and Maarten Krol. Interpretation of field observations of point-source methane plume using observation-driven large-eddy simulations. *Atmospheric Chemistry and Physics*, 22(10):6489–6505, 2022.

[22] Apisada Chulakadabba, Maryann Sargent, Thomas Lauvaux, Joshua S Benmergui, Jonathan E Franklin, Christopher Chan Miller, Jonas S Wilzewski, Sébastien Roche, Eamon Conway, Amir H Souri, et al. Methane point source quantification using methaneair: a new airborne imaging spectrometer. *Atmospheric Measurement Techniques*, 16(23):5771–5785, 2023.

[23] Pablo E Saide, Daniel F Steinhoff, Branko Kosovic, Jeffrey Weil, Nicole Downey, Doug Blewitt, Steven R Hanna, and Luca Delle Monache. Evaluating methods to estimate methane emissions from oil and gas production facilities using les simulations. *Environmental Science & Technology*, 52(19):11206–11214, 2018.

[24] Lilian Joly, Rabih Maamary, Thomas Decarpenterie, Julien Cousin, Nicolas Dumelié, Nicolas Chauvin, Dominique Legain, Diane Tzanos, and Georges Durry. Atmospheric measurements by ultra-light spectrometer (amulse) dedicated to vertical profile in situ measurements of carbon dioxide (co2) under weather balloons: Instrumental development and field application. *Sensors*, 16(10):1609, 2016.

[25] Lilian Joly, Olivier Coopmann, Vincent Guidard, Thomas Decarpenterie, Nicolas Dumelié, Julien Cousin, Jérémie Burgalat, Nicolas Chauvin, Grégory Albora, Rabih Maamary, et al. The development of the atmospheric measurements by ultra-light spectrometer (amulse) greenhouse gas profiling system and application for satellite retrieval validation. *Atmospheric Measurement Techniques*, 13(6):3099–3118, 2020.

[26] Pramod Kumar, Grégoire Broquet, Christopher Caldow, Olivier Laurent, Susan Gichuki, Ford Cropley, Camille Yver-Kwok, Bonaventure Fontanier, Thomas Lauvaux, Michel Ramonet, et al. Near-field atmospheric inversions for the localization and quantification of controlled methane releases using stationary and mobile measurements. *Quarterly Journal of the Royal Meteorological Society*, 148(745):1886–1912, 2022.

[27] Noah L Ryder, Jason A Sutula, Christopher F Schemel, Andrew J Hamer, and Vincent Van Brunt. Consequence modeling using the fire dynamics simulator. *Journal of hazardous materials*, 115(1-3):149–154, 2004.

[28] Wolfram Jahn, Guillermo Rein, and Jose Torero. The effect of model parameters on the simulation of fire dynamics. *Fire Safety Science*, pages 1341–1352, 2008.

[29] Esther Kim, John P Woycheese, and Nicholas A Dembsey. Fire dynamics simulator (version 4.0) simulation for tunnel fire scenarios with forced, transient, longitudinal ventilation flows. *Fire Technology*, 44(2):137–166, 2008.

[30] Hamidreza Ardeshiri, Massimo Cassiani, Soon Young Park, Andreas Stohl, Ignacio Pisso, and Anna Solvejg Dinger. On the convergence and capability of the large-eddy simulation of concentration fluctuations in passive plumes for a neutral boundary layer at infinite reynolds number. *Boundary-Layer Meteorology*, 176(3):291–327, 2020.

[31] NASA JPL. Nasa shuttle radar topography mission global 3 arc second number netcdf. *NASA EOSDIS Land Processes Distributed Active Archive Center (DAAC) data set*, pages SRTMGL3_NUMNC–003, 2013.

[32] Rakesh Yuvaraj, Thomas Lauvaux, Charbel Abdallah, Philippe Ciais, Julian Akani Guery, Jean-Louis Bonne, Alexis Groshenry, Ngoc Minh Hoang, and Lilian Joly. High-resolution modelling of methane plumes: validation and sensitivity experiments to explore emission quantification approaches. ChemRxiv preprint DOI:10.26434/chemrxiv-2025-lv32x, available at https://chemrxiv.org/engage/chemrxiv/article-details/690dcfc8113cc7cfffb7d85c, 2025.